Low-Frequency Stability Analysis of Inverter-Based Islanded Multiple-Bus AC Microgrids Based on Terminal Characteristics

Journal:	*IEEE Transactions on Smart Grid*
Manuscript ID	TSG-01738-2018.R1
Manuscript Type:	Transactions
Date Submitted by the Author:	11-May-2019
Complete List of Authors:	Cao, Wenchao; Danfoss Turbocor Compressors, Inc. ma, yiwei; The University of Tennessee, Knoxville, Wang, Fred; The University of Tennessee, Knoxville, Department of Electrical Engineering and Computer Science Tolbert, Leon; The University of Tennessee, Electrical and Computer Engineering; Oak Ridge National Laboratory, Power Electronics and Electric Machinery Research Center Xue, Yaosuo; Oak Ridge National Laboratory, Electrical & Electronics System Research Division
Technical Topic Area :	Microgrids (planning, operation, control, islanding, protection) < Transactions on Smart Grid, Active Distribution Networks (distributed resources, energy efficiency, economics, reliability) < Transactions on Smart Grid
Key Words:	Inverters, Stability criteria, Impedance, Power electronics, Resonance

Low-Frequency Stability Analysis of Inverter-Based Islanded Multiple-Bus AC Microgrids Based on Terminal Characteristics

Wenchao Cao, *Member, IEEE*, Yiwei Ma, *Student Member, IEEE*, Fred Wang, *Fellow, IEEE*, Leon M. Tolbert, *Fellow, IEEE*, and Yaosuo Xue, *Senior Member, IEEE*

***Abstract*—For system planning of three-phase inverter-based islanded ac microgrids, the low frequency instability issue caused by interactions of inverter droop controllers is a major concern. When internal control information of procured commercial inverters is unknown, impedance-based small-signal stability criteria facilitate prediction of resonances in medium and high frequency ranges, but they usually assume the grid fundamental frequency as constant and thus they are incapable of analyzing the low-frequency oscillation of the fundamental frequency in islanded microgrids. Aiming at solving this issue, this paper proposes two stability analysis methods based on terminal characteristics of inverters and passive connection network including the dynamics of the fundamental frequency for analysis of low-frequency stability in islanded multiple-bus microgrids. Based on the Component Connection Method (CCM) to systematically separate inverters from the passive connection network, a general approach is developed to model the microgrid as a multiple-input-multiple-output (MIMO) negative feedback system in the common system *d-q* reference frame. By applying the generalized Nyquist stability criterion (GNC) to the return-ratio and return-difference matrices of the MIMO system model, the low-frequency stability related to the fundamental frequency can be analyzed using the measured terminal characteristics of inverters. Analysis and simulation of a 37-bus microgrid verify the effectiveness of the proposed stability analysis methods.**

***Index Terms*—Ac microgrids, droop control, impedance, inverters, small-signal stability, terminal characteristics.**

I. Introduction

MICROGRIDS can improve the efficiency and reliability of power systems by coordinating distributed generation (DG) units, energy storages, and local loads to achieve autonomous operation [1]. Three-phase power electronics inverters are increasingly common as interfaces of components within ac microgrids for efficient and flexible power conversion. The small-signal stability analysis of three-phase inverter-based islanded ac microgrids utilizing eigenvalues of complete system state-space models reveals frequency-scale separation among system modes [2]. The medium and high frequency modes are correlated with the fast inner current and voltage control loops of inverters and passive elements, while the low-frequency modes have a close relationship with the slow outer power control loop by means of frequency and voltage droop controls for power sharing [3]–[6].

For the low-frequency stability analysis of inverter-based islanded multiple-bus microgrids, the detailed state-space small-signal models developed in [2] suffer from high complexity with increase in system size. Therefore, model order reduction methods, such as time-scale separation and singular perturbations, were proposed to simplify the analysis [7], [8]. The Component Connection Method (CCM) was also applied to the state-space matrix to create sparsity and reduce the computational burden [9]. Another drawback of the state-space-based approach is the necessity for detailed internal control information of inverters, which is nevertheless usually unavailable in practical applications [10]. An alternative small-signal stability analysis method, the impedance-based approach [12], [13], can assess the medium and high frequency stability of multiple-bus microgrids on the basis of inverter impedances [14], [15], which are measurable frequency responses of voltage and current at inverter terminals without the need for internal control information [16], [17]. However, inverter impedances usually assume constant grid fundamental frequency, so they are inapplicable to the low-frequency stability analysis of droop control in islanded microgrids where the fundamental frequency is not constant but dynamically regulated.

To enable the impedance-based approach for the low-frequency stability analysis, the frequency-domain terminal characteristics modeling of system components should be expanded to further include the grid fundamental frequency as a variable [18]. Such terminal characteristics models of three-phase droop-controlled inverters and current-controlled inverters were developed in [18] and [19], based on which a stability criterion was proposed in [20] and [21] for a simple single-bus microgrid with multiple droop-controlled inverters in parallel sharing a common constant-current load. However, terminal characteristics models with the fundamental frequency variable for passive components, such as transmission lines, passive loads and shunt capacitors, have not been discussed in the literature yet. In addition, the low-

W. Cao is with Danfoss Turbocor Compressors, Inc., Tallahassee, FL 32310 USA (email: wcao2@vols.utk.edu).

Y. Ma, F. Wang, and L. M. Tolbert are with the Min H. Kao Department of Electrical Engineering and Computer Science, The University of Tennessee, Knoxville, TN 37996-2250 USA (e-mail: yma13@vols.utk.edu; fred.wang@utk.edu; tolbert@utk.edu).

Y. Xue is with the Electrical & Electronics System Research Division, Oak Ridge National Laboratory, Oak Ridge, TN 37831 USA (e-mail: xuey@ornl.gov).

frequency stability analysis of islanded multiple-bus microgrids based on terminal characteristics of network components remains an unsolved challenge.

The Component Connection Method (CCM) in the frequency domain [22] and the generalized Nyquist stability criterion (GNC) [23], [24] were applied to the impedance-based approach in [15] to effectively analyze stability related to medium and high frequency modes of three-phase inverter-based multiple-bus ac power systems. With the aim of filling in the aforementioned gaps about the low-frequency stability analysis, this paper expands the work in [15] and further proposes two stability analysis methods on the basis of components' terminal characteristics including the frequency response of the system fundamental frequency. In addition to the inverters, the terminal characteristics of passive components are also derived. A general approach based on the CCM is developed to derive the terminal-characteristics matrix of the connection network and establish the terminal-characteristics-based models of islanded multiple-bus ac microgrid systems. By applying the GNC to the return-ratio and return-difference matrices of the system model, the proposed stability analysis methods are capable of analyzing the low-frequency stability of inverter-based islanded multiple-bus ac microgrids without requiring internal information of inverters.

II. System Description

The IEEE 37-bus test system described in [25] has been modified as a three-phase inverter-based multiple-bus islanded ac microgrid. There are 25 *RL* loads, 3 shunt capacitors (C_p) and 7 inverters: 4 voltage-controlled inverters (VI1−VI4) with outer droop control and 3 current-controlled inverters (CI1−CI3) with outer constant power control, as illustrated in Fig. 1. The network branches and loads have the same parameters as listed in Tables V and VI in [25]. The shunt capacitors are C_{p1}=150 μF, C_{p2}=300 μF and C_{p3}=100 μF, respectively. Table I provides the inverter parameters [15].

The one-line diagram of the three-phase inverter with a *L* filter connected to the slack bus through a line impedance Z_{Line} is depicted in Fig. 2. i_t, v_M and v_t are the output current and output voltages before and after the *L* filter of the inverter, respectively. The dc-link voltage V_{dc} is assumed constant. v_s is the slack bus voltage. For system-level modeling and analysis, two kinds of synchronous *d-q* reference frames should be distinguished. Each inverter is controlled in its own local terminal *d-q* reference frame with the superscript *c*. The system stability should be analyzed in a common system *d-q* reference frame with the superscript *s*. It is a common practice to arbitrarily choose one inverter terminal *d-q* reference frame as the common system *d-q* reference frame. For the studied system, the terminal *d-q* reference frame of inverter VI1 at Bus 34 is selected for this purpose [2], [20]. ω^c and θ^c are the angular frequency and angle of the inverter *d-q* frame with respect to phase-a, while ω^s and θ^s are the angular frequency and angle of the common system *d-q* frame with respect to phase-a. δ denotes the angle difference between these two *d-q* frames, as derived in (1), where δ_0 is the steady-state angle difference. Based on the reference frame transformation technique [2], the transformation $\mathbf{T}(\delta)$ from the common *d-q* frame to the inverter *d-q* frame is shown in (2).

$$\delta = \theta^c - \theta^s = \delta_0 + \int \left(\omega^c - \omega^s\right) dt \tag{1}$$

$$\mathbf{T}(\delta) = \begin{bmatrix} \cos\delta & \sin\delta \\ -\sin\delta & \cos\delta \end{bmatrix} \tag{2}$$

It is worth noting that each droop-controlled inverter actively regulates its local angular frequency and collaboratively results in a consequent balanced system angular frequency in the steady state. Selection of the output frequency of one inverter (VI1 in this example) as the common system fundamental frequency is only for easy analysis of the system.

Fig. 3(a) shows the control block diagram for the current-controlled inverters (CI1−CI3), and the input reference vector of the power controller is $\vec{i}^{\,*}=[P_0\ Q_0]^{\mathrm{T}}$, where P_0 and Q_0 are set points of active and reactive power as presented in Table II.

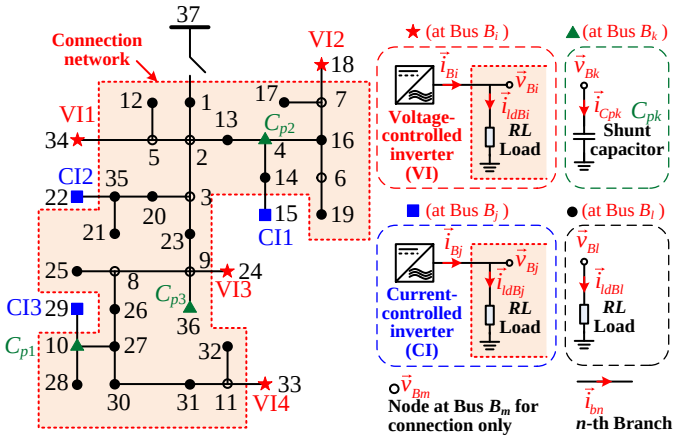

Fig. 1. Diagram of the modified IEEE 37-bus system in the islanded mode.

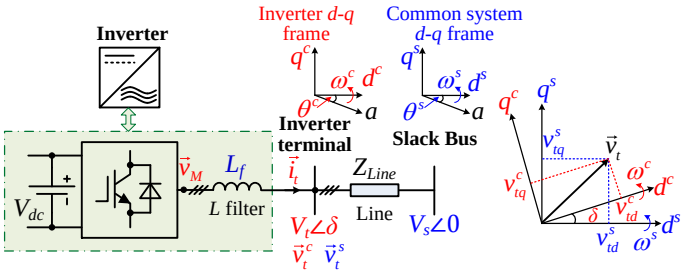

Fig. 2. Block diagram of a three-phase inverter with an output *L* filter, and the relationship between different *d-q* reference frames.

TABLE I
Parameters of Inverters

Common Parameters		Values
L filter per phase $L_f s + R_{Lf}$	L_f R_{Lf}	0.575 mH 0.2 Ω
Dc-link voltage	V_{dc}	130 V
Switching frequency	f_s	10 kHz
Switching period	T_s	100 μs
Current-Controlled Inverters		**Values**
Current PI controller $\mathbf{G_c} = (K_{cp} + K_{ci}/s)\mathbf{I}$	K_{cp} K_{ci}	2.6 2275
Voltage feed-forward $\mathbf{G_{ffv}}$	ω_{ffv}	50×2π rad/s
PLL PI controller $K_{PLLp} + K_{PLLi}/s$	K_{PLLp} K_{PLLi}	1.06 18
Voltage-Controlled Inverters		**Values**

Voltage PI controller $\mathbf{G_v} = (K_{vp} + K_{vi}/s)\mathbf{I}$	K_{vp}	1.04
	K_{vi}	325
Current filter $\mathbf{G_{fc}}$ in current feed-forward	ω_{fc}	1000×2π rad/s
Voltage filter $\mathbf{G_{fv}}$	ω_{fv}	300×2π rad/s

TABLE II
INVERTERS PARAMETERS OF THE MODIFIED IEEE 37-BUS SYSTEM

Inverter	P_0 (W)	Q_0 (Var)	V_0 (V)	ω_0 (rad/s)	m_P	n_Q
VI1−VI4	250	0	50	60×2π	0.0025	0.0067
CI1−CI3	250	150	n/a	n/a	n/a	n/a

Fig. 3(b) shows the control block diagram for the voltage-controlled inverters (VI1−VI4), and the droop controller has the input reference vector $\vec{v}^* = [\omega_0\ V_0\ P_0\ Q_0]^T$, where ω_0 and V_0 are set points of voltage and frequency as given in Table II. Fig. 3(c) depicts the detailed diagram of the droop controller adopted by inverters (VI1−VI4). The instantaneous real power p and reactive power q are calculated from the measured inverter terminal voltage $\vec{v}_t^{\,c}$ and current $\vec{i}_t^{\,c}$ in the inverter d-q frame. The average real power P and reactive power Q are

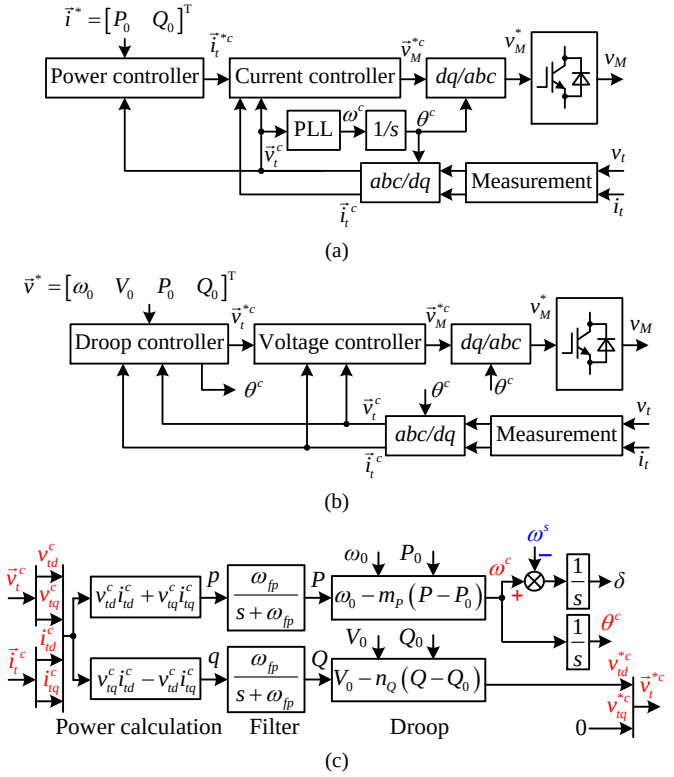

Fig. 3. Control block diagrams of inverters: (a) inverters with inner current loop and outer power loop, (b) inverters with inner voltage loop and outer droop loop, and (c) detailed diagram of the droop controller.

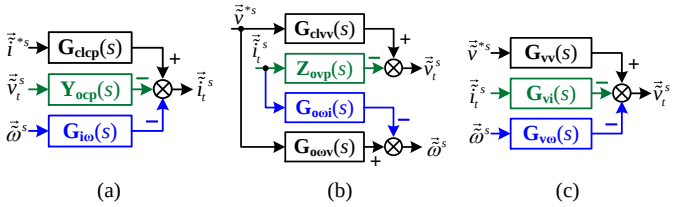

Fig. 4. Small-signal block diagrams of inverters based on terminal characteristics in the common system d-q frame: (a) current-controlled inverter, (b) voltage-controlled inverter which provides the common system fundamental frequency ω^s, and (c) other voltage-controlled inverters.

obtained by using low-pass filters (LPF) with a cut-off frequency $\omega_{fp} = 5\times 2\pi$ rad/s. Then based on the droop equations in (3), the inverter frequency reference ω^c and the voltage references (v_{td}^{*c} and v_{tq}^{*c}) in the inverter d-q frame are generated, according to the nominal set points of P_0, Q_0, V_0 and ω_0 as well as the droop coefficients (m_P and n_Q) as listed in Table II. Detailed modeling of inner current and voltage control loops can be found in [15].

$$\omega^c = \omega_0 - m_P(P - P_0),\ v_{td}^{*c} = V_0 - n_Q(Q - Q_0),\ v_{tq}^{*c} = 0 \quad (3)$$

III. TERMINAL-CHARACTERISTICS MODELING AND MEASUREMENT OF THREE-PHASE INVERTERS

A. Terminal-Characteristics Modeling

By defining the inverter output current vector $\vec{i}_t^{\,s}$ and the terminal voltage vector $\vec{v}_t^{\,s}$ in the common system d-q frame and introducing the fundamental angular frequency vector $\vec{\omega}^s$ as expressed in (4) [18], Fig. 4 depicts the small-signal block diagrams of inverters based on terminal characteristics in the common system d-q frame. For the current-controlled inverters (CI1−CI3) with outer power control loop as shown in Fig. 4(a), the complete small-signal model can be expressed as (5), where $\mathbf{G_{clcp}}(s)$ is the current closed-loop gain, $\mathbf{Y_{ocp}}(s)$ is the closed-loop output d-q admittance, and $\mathbf{G_{i\omega}}(s)$ is the closed-loop frequency-to-current transfer function matrix, as expressed in (6). The top symbol "~" denotes small signal.

$$\vec{i}_t^{\,s} = \begin{bmatrix} i_{td}^s & i_{tq}^s \end{bmatrix}^T,\quad \vec{v}_t^{\,s} = \begin{bmatrix} v_{td}^s & v_{tq}^s \end{bmatrix}^T,\quad \vec{\omega}^s = \begin{bmatrix} \omega^s & 0 \end{bmatrix}^T \quad (4)$$

$$\tilde{\vec{i}}_t^{\,s} = \mathbf{G_{clcp}}(s)\tilde{\vec{i}}^{*s} - \mathbf{Y_{ocp}}(s)\tilde{\vec{v}}_t^{\,s} - \mathbf{G_{i\omega}}(s)\tilde{\vec{\omega}}^s \quad (5)$$

$$\mathbf{Y_{ocp}}(s) = \begin{bmatrix} Y_{ocp\_dd}(s) & Y_{ocp\_dq}(s) \\ Y_{ocp\_qd}(s) & Y_{ocp\_qq}(s) \end{bmatrix},\ \mathbf{G_{i\omega}}(s) = \begin{bmatrix} G_{i\omega\_d}(s) & 0 \\ G_{i\omega\_q}(s) & 0 \end{bmatrix} \quad (6)$$

For the voltage-controlled inverter with outer droop control loop (VI1 is selected in this study), which provides the common system fundamental frequency ω^s as shown in Fig. 4(b), the complete small-signal model can be expressed as (7), where $\mathbf{G_{clvv}}(s)$ is the voltage closed-loop gain, $\mathbf{Z_{ovp}}(s)$ is the closed-loop output d-q impedance, and $\mathbf{G_{o\omega i}}(s)$ and $\mathbf{G_{o\omega v}}(s)$ are the closed-loop current-to-frequency transfer function matrix and the reference-to-frequency transfer function matrix, respectively, as expressed in (8).

$$\begin{cases} \tilde{\vec{v}}_t^{\,s} = \mathbf{G_{clvv}}(s)\tilde{\vec{v}}^{*s} - \mathbf{Z_{ovp}}(s)\tilde{\vec{i}}_t^{\,s} \\ \tilde{\vec{\omega}}^s = \mathbf{G_{o\omega v}}(s)\tilde{\vec{v}}^{*s} - \mathbf{G_{o\omega i}}(s)\tilde{\vec{i}}_t^{\,s} \end{cases} \quad (7)$$

$$\begin{cases} \mathbf{Z_{ovp}}(s) = \begin{bmatrix} Z_{ovp\_dd}(s) & Z_{ovp\_dq}(s) \\ Z_{ovp\_qd}(s) & Z_{ovp\_qq}(s) \end{bmatrix},\quad \mathbf{G_{o\omega i}}(s) = \begin{bmatrix} G_{o\omega i\_d}(s) & G_{o\omega i\_q}(s) \\ 0 & 0 \end{bmatrix} \\ \mathbf{G_{o\omega v}}(s) = \begin{bmatrix} G_{o\omega v\_d}(s) & G_{o\omega v\_q}(s) \\ 0 & 0 \end{bmatrix} \end{cases} \quad (8)$$

For other voltage-controlled inverters (VI2−VI4) with outer droop control loop as shown in Fig. 4(c), the complete small-signal model can be expressed as (9), where $\mathbf{G_{vv}}(s)$ is the voltage closed-loop gain, $\mathbf{G_{vi}}(s)$ is the closed-loop output d-q impedance, and $\mathbf{G_{v\omega}}(s)$ is the closed-loop frequency-to-voltage transfer function matrix as expressed in (10).

$$\vec{\tilde{v}}_t^{\,s} = \mathbf{G_{vv}}(s)\vec{\tilde{v}}^{*s} - \mathbf{G_{vi}}(s)\vec{\tilde{i}}_t^{\,s} - \mathbf{G_{v\omega}}(s)\vec{\tilde{\omega}}^{s} \quad (9)$$

$$\mathbf{G_{vi}}(s) = \begin{bmatrix} G_{vi\_dd}(s) & G_{vi\_dq}(s) \\ G_{vi\_qd}(s) & G_{vi\_qq}(s) \end{bmatrix}, \mathbf{G_{v\omega}}(s) = \begin{bmatrix} G_{v\omega\_d}(s) & 0 \\ G_{v\omega\_q}(s) & 0 \end{bmatrix} \quad (10)$$

Detailed analytical expressions can be obtained by generally following the approach in [18] and [19]. But the terminal characteristics of inverters can also be measured to obviate the need for internal control information of inverters.

B. Terminal-Characteristics Measurement

The basic principle of terminal-characteristics measurement is still based on injection of small sinusoidal perturbation signals with certain frequency ω_{inj}, measurement of responses of the inverter under test at the desired operating condition, and calculation of frequency responses by using fast Fourier transform (FFT). Its difference from the normal impedance measurement techniques as presented in [16] is that the common system fundamental frequency ω^s should be further treated as a perturbation signal for measurement of CI1−CI3 and VI2−VI4 or a response signal for measurement of VI1.

Fig. 5(a) shows the setup for terminal-characteristics measurement of current-controlled inverters (CI1−CI3). A three-phase controlled voltage source is adopted not only for generating the three-phase voltage at the fundamental frequency ω^s to establish the desired operating condition for the inverter under test, but also for injecting three perturbation signals, including the voltage perturbation signals (v_{pd}^s and v_{pq}^s) in the common system *d-q* frame and the perturbation signal of the common system fundamental frequency ω_p^s. The terminal voltage v_t and current i_l of the inverter under test are measured and transformed to the values in the common system *d-q* frame, namely, v_{td}^s, v_{tq}^s, i_{ld}^s and i_{lq}^s.

To solve six unknown values in the terminal characteristics $\mathbf{Y_{ocp}}(j\omega)$ and $\mathbf{G_{i\omega}}(j\omega)$ of a current-controlled inverter, three groups of independent perturbations with the subscripts 1, 2 and 3, respectively, are required, as expressed in (11) for example. Then, the terminal characteristics can be calculated as (12). By sweeping the frequency of the injected signals and repeating the measurement process, the frequency response of the terminal characteristics of a current-controlled inverter in the desired frequency range can be obtained.

$$\begin{cases} v_{pd1}^s \neq 0, & v_{pq1}^s = 0, & \omega_{p1}^s = 0 \\ v_{pd2}^s = 0, & v_{pq2}^s \neq 0, & \omega_{p2}^s = 0 \\ v_{pd3}^s = 0, & v_{pq3}^s = 0, & \omega_{p3}^s \neq 0 \end{cases} \quad (11)$$

$$\begin{bmatrix} Y_{ocp\_dd} & Y_{ocp\_dq} & G_{i\omega\_d} \\ Y_{ocp\_qd} & Y_{ocp\_qq} & G_{i\omega\_q} \end{bmatrix} = \begin{bmatrix} i_{ld1}^s & i_{ld2}^s & i_{ld3}^s \\ i_{lq1}^s & i_{lq2}^s & i_{lq3}^s \end{bmatrix} \cdot \begin{bmatrix} v_{td1}^s & v_{td2}^s & v_{td3}^s \\ v_{tq1}^s & v_{tq2}^s & v_{tq3}^s \\ \omega_{p1}^s & \omega_{p2}^s & \omega_{p3}^s \end{bmatrix}^{-1} \quad (12)$$

Similarly, Fig. 5(b) shows the setup for terminal-characteristics measurement of voltage-controlled inverters (VI1−VI4). A three-phase passive *RLC* load is used to make the inverter under test operate in the desired operating point. Another three-phase shunt controlled current source is utilized to inject current perturbations. For VI1 which provides the common system fundamental frequency ω^s, perturbation signals include the currents (i_{pd}^s and i_{pq}^s) in the common system *d-q* frame. The measured signals include the common system fundamental frequency ω^s and the terminal voltages and currents (v_{td}^s, v_{tq}^s, i_{sd}^s and i_{sq}^s) of the inverter under test in the common system *d-q* frame. Through two independent perturbations, the terminal characteristics of VI1 can be obtained as (13). For VI2−VI4, the common system fundamental frequency ω_p^s becomes another perturbation signal, and their terminal characteristics can be solved as (14), by three independent perturbations.

$$\begin{bmatrix} Z_{ovp\_dd} & Z_{ovp\_dq} \\ Z_{ovp\_qd} & Z_{ovp\_qq} \\ G_{o\omega i\_d} & G_{o\omega i\_q} \end{bmatrix} = \begin{bmatrix} v_{td1}^s & v_{td2}^s \\ v_{tq1}^s & v_{tq2}^s \\ \omega_1^s & \omega_2^s \end{bmatrix} \cdot \begin{bmatrix} i_{sd1}^s & i_{sd2}^s \\ i_{sq1}^s & i_{sq2}^s \end{bmatrix}^{-1} \quad (13)$$

$$\begin{bmatrix} G_{vi\_dd} & G_{vi\_dq} & G_{v\omega\_d} \\ G_{vi\_qd} & G_{vi\_qq} & G_{v\omega\_q} \end{bmatrix} = \begin{bmatrix} v_{td1}^s & v_{td2}^s & v_{td3}^s \\ v_{tq1}^s & v_{tq2}^s & v_{tq3}^s \end{bmatrix} \cdot \begin{bmatrix} i_{sd1}^s & i_{sd2}^s & i_{sd3}^s \\ i_{sq1}^s & i_{sq2}^s & i_{sq3}^s \\ \omega_{p1}^s & \omega_{p2}^s & \omega_{p3}^s \end{bmatrix}^{-1} \quad (14)$$

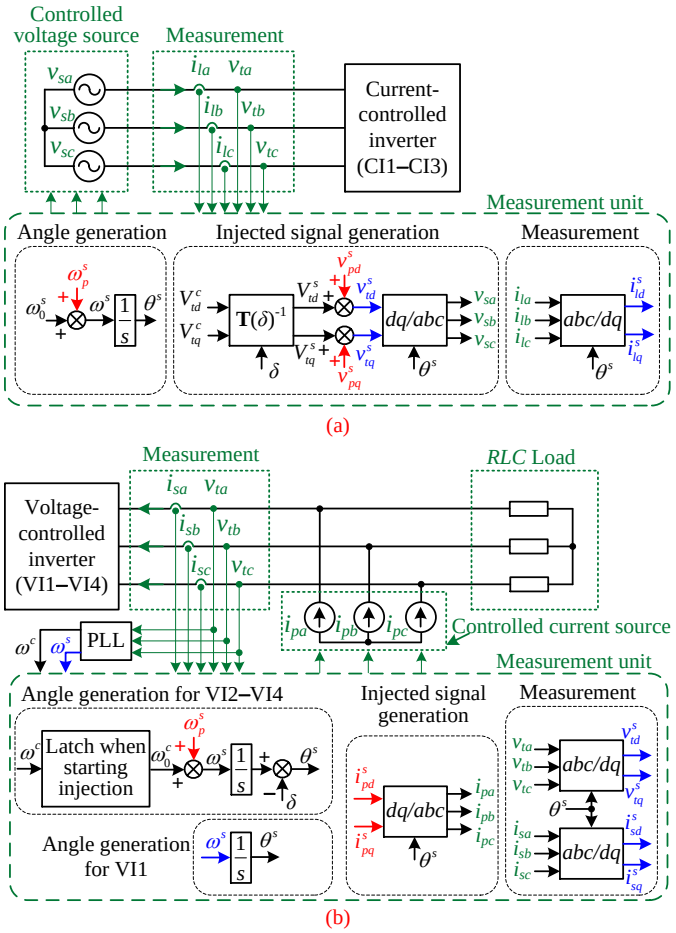

Fig. 5. Terminal-characteristics measurement setups: (a) for current-controlled inverters, and (b) for voltage-controlled inverters.

Fig. 6, Fig. 7, and Fig. 8 present the Bode plots of the measured terminal characteristics of the current-controlled inverter CI1, the droop-controlled inverter VI1 which is chosen to provide ω^s and the droop-controlled inverter VI2, respectively, in the simulation using MATLAB/Simulink. The injection frequency ω_{inj} for measurement sweeps from 1 Hz to

5 kHz with 100 logarithmically spaced points.

The impact of the droop controller parameters on the terminal characteristics of voltage-controlled inverters with the outer droop control loop is investigated by the measured terminal characteristics. Two cases with different droop controller parameters are considered, namely, Case 1: m_P = 0.0025 and n_Q = 0.0067, and Case 2: m_P = 0.0050 and n_Q = 0.0133. It can be observed that the droop parameters mainly influence the terminal characteristics of the droop-controlled inverters (VI1 and VI2) in the low-frequency range below 100 Hz. In addition, larger droop parameter values would result in larger magnitudes of the terminal characteristics.

It should be noted that terminal characteristics measurement approach described here is similar to the measurement approach presented in [21], the accuracy of which has been verified by the agreement between the measurement results and the analytical calculation results in [18]. Since this measurement approach is not the focus of this paper, the measurement results in Fig. 6 to Fig. 8 are not compared with the analytical transfer functions.

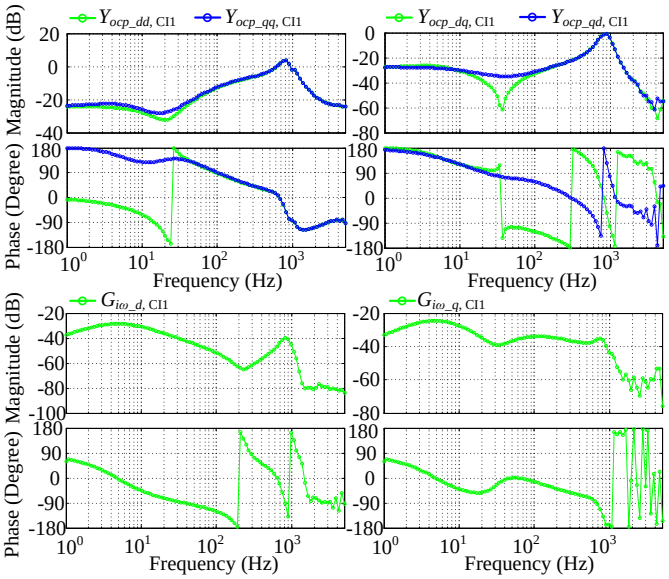

Fig. 6. Bode plots of the terminal characteristics of the current-controlled inverter CI1.

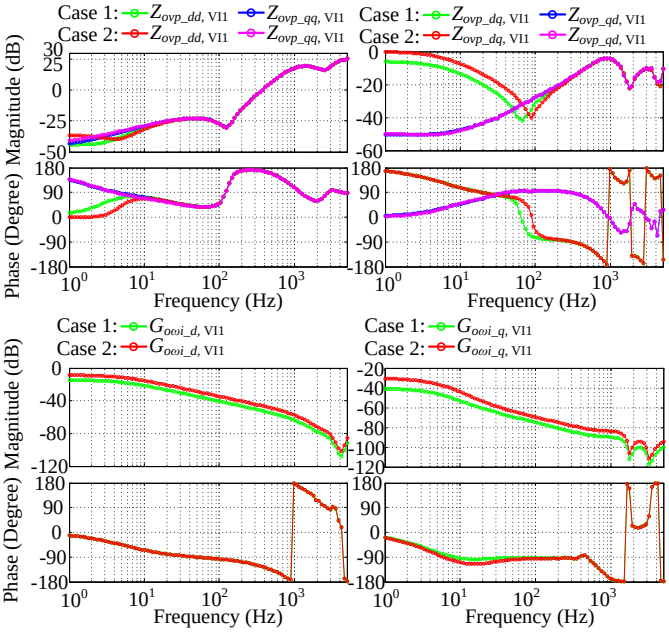

Fig. 7. Bode plots of the terminal characteristics of the droop-controlled inverter VI1.

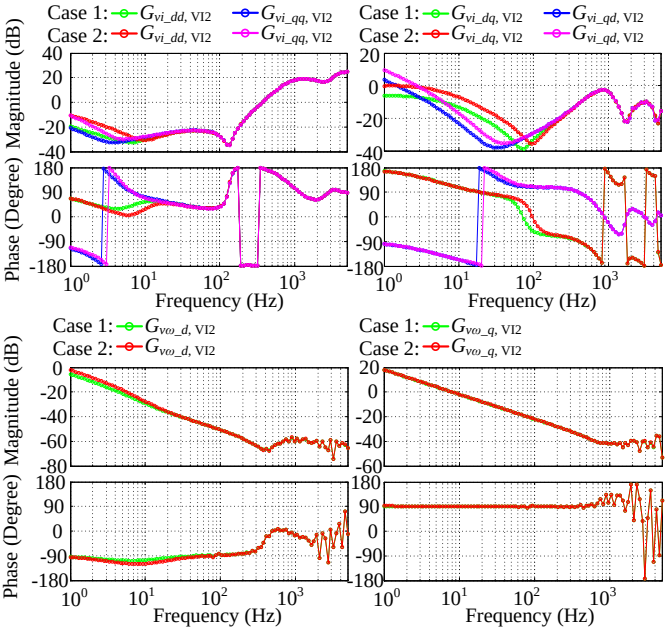

Fig. 8. Bode plots of the terminal characteristics of the droop-controlled inverter VI2.

IV. Proposed Stability Analysis Methods

A. System Model Based on the CCM

The Component Connection Method (CCM) [22] separates the inverters from the passive connection network, and thus it provides a general way to decompose the inverter-based islanded ac microgrids with complicated structures [15]. The decomposition of the microgrid is illustrated in Fig. 1.

On the one hand, all inverters can be modeled collectively as follows. Only the frequency of one droop-controlled inverter (VI1) is selected as the common system fundamental frequency ω^s, and all other droop-controlled inverters and current-controlled inverters are modeled or measured in the

common system *d-q* reference frame. Therefore, VI1 can be separated at first to facilitate the modeling, while all other inverters can be modeled in a composite model as expressed in (15). The output vector $\vec{Y}(s)$, reference vector $\vec{U}(s)$, and disturbance vector $\vec{D}(s)$ of inverters are expressed in (16), respectively. $\mathbf{G_{cl}}(s)$ is the closed-loop transfer function matrix from the reference to the output as described in (17). $\mathbf{G_{cd}}(s)$ is the closed-loop transfer function matrix from the disturbance to the output with inverter output impedances or admittances as the diagonal elements, as shown in (18). $\mathbf{G_{c\omega}}(s)$ is the closed-loop transfer function matrix from the common system fundamental frequency to the output with the fundamental-frequency-related terminal characteristics of inverters as the diagonal elements, as shown in (19).

$$\vec{Y}(s)=\mathbf{G_{cl}}(s)\vec{U}(s)-\mathbf{G_{cd}}(s)\vec{D}(s)-\mathbf{G_{c\omega}}(s)\vec{\tilde{\omega}}^{s}(s) \quad (15)$$

$$\begin{cases}\vec{Y}(s)=[\vec{\tilde{v}}^{s}_{t,\mathrm{VI2}}(s),\vec{\tilde{v}}^{s}_{t,\mathrm{VI3}}(s),\vec{\tilde{v}}^{s}_{t,\mathrm{VI4}}(s),\vec{\tilde{i}}^{s}_{t,\mathrm{CI1}}(s),\vec{\tilde{i}}^{s}_{t,\mathrm{CI2}}(s),\vec{\tilde{i}}^{s}_{t,\mathrm{CI3}}(s)]^{\mathrm{T}}\\ \vec{U}(s)=[\vec{\tilde{v}}^{*s}_{\mathrm{VI2}}(s),\vec{\tilde{v}}^{*s}_{\mathrm{VI3}}(s),\vec{\tilde{v}}^{*s}_{\mathrm{VI4}}(s),\vec{\tilde{i}}^{*s}_{\mathrm{CI1}}(s),\vec{\tilde{i}}^{*s}_{\mathrm{CI2}}(s),\vec{\tilde{i}}^{*s}_{\mathrm{CI3}}(s)]^{\mathrm{T}}\\ \vec{D}(s)=[\vec{\tilde{i}}^{s}_{t,\mathrm{VI2}}(s),\vec{\tilde{i}}^{s}_{t,\mathrm{VI3}}(s),\vec{\tilde{i}}^{s}_{t,\mathrm{VI4}}(s),\vec{\tilde{v}}^{s}_{t,\mathrm{CI1}}(s),\vec{\tilde{v}}^{s}_{t,\mathrm{CI2}}(s),\vec{\tilde{v}}^{s}_{t,\mathrm{CI3}}(s)]^{\mathrm{T}}\end{cases} \quad (16)$$

$$\mathbf{G_{cl}}=\mathrm{diag}[\mathbf{G_{vv,VI2}},\mathbf{G_{vv,VI3}},\mathbf{G_{vv,VI4}},\mathbf{G_{clcp,CI1}},\mathbf{G_{clcp,CI2}},\mathbf{G_{clcp,CI3}}] \quad (17)$$

$$\mathbf{G_{cd}}=\mathrm{diag}[\mathbf{G_{vi,VI2}},\mathbf{G_{vi,VI3}},\mathbf{G_{vi,VI4}},\mathbf{Y_{ocp,CI1}},\mathbf{Y_{ocp,CI2}},\mathbf{Y_{ocp,CI3}}] \quad (18)$$

$$\mathbf{G_{c\omega}}=[\mathbf{G_{v\omega,VI2}}^{\mathrm{T}},\mathbf{G_{v\omega,VI3}}^{\mathrm{T}},\mathbf{G_{v\omega,VI4}}^{\mathrm{T}},\mathbf{G_{i\omega,CI1}}^{\mathrm{T}},\mathbf{G_{i\omega,CI2}}^{\mathrm{T}},\mathbf{G_{i\omega,CI3}}^{\mathrm{T}}]^{\mathrm{T}} \quad (19)$$

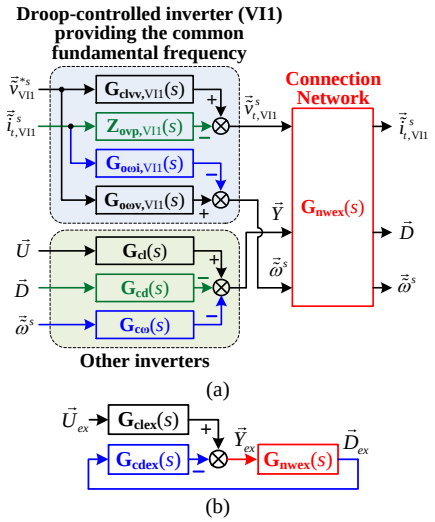

Fig. 9. Small-signal diagrams of the CCM applied to the inverter-based microgrid: (a) detailed diagram, and (b) equivalent MIMO feedback system.

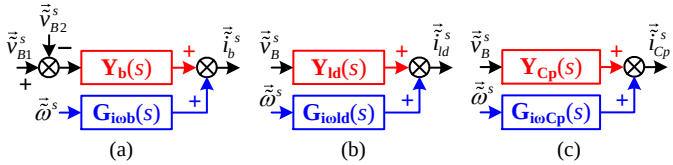

Fig. 10. Small-signal block diagrams of passive components in the common system *d-q* frame: (a) a branch, (b) a *RL* load, and (c) a shunt capacitor.

Then, the model of the inverter VI1 can be further combined with the composite model of all other inverters to create the extended composite model of all inverters, by including the common system fundamental frequency vector $\vec{\tilde{\omega}}^{s}$ in both the extended output vector $\vec{Y}_{ex}(s)$ and the extended disturbance vector $\vec{D}_{ex}(s)$, and the extended reference vector $\vec{U}_{ex}(s)$ is also defined accordingly, as expressed in (20). Correspondingly, the extended closed-loop transfer function matrix from the reference to the output $\mathbf{G_{clex}}(s)$ is derived in (21), and the extended closed-loop transfer function matrix from the disturbance to the output $\mathbf{G_{cdex}}(s)$ is derived in (22).

$$\begin{cases}\vec{Y}_{ex}(s)=[\vec{\tilde{v}}^{s}_{t,\mathrm{VI1}}(s),\vec{Y}(s),\vec{\tilde{\omega}}^{s}(s)]^{\mathrm{T}},\vec{U}_{ex}(s)=[\vec{\tilde{v}}^{*s}_{\mathrm{VI1}}(s),\vec{U}(s),\vec{\tilde{v}}^{*s}_{\mathrm{VI1}}(s)]^{\mathrm{T}}\\ \vec{D}_{ex}(s)=[\vec{\tilde{i}}^{s}_{t,\mathrm{VI1}}(s),\vec{D}(s),\vec{\tilde{\omega}}^{s}(s)]^{\mathrm{T}}\end{cases} \quad (20)$$

$$\mathbf{G_{clex}}(s)=\mathrm{diag}[\mathbf{G_{clvv,VI1}}(s),\mathbf{G_{cl}}(s),\mathbf{G_{o\omega v,VI1}}(s)] \quad (21)$$

$$\mathbf{G_{cdex}}(s)=\begin{bmatrix}\mathbf{Z_{ovp,VI1}}(s) & \mathbf{0} & \mathbf{0}\\ \mathbf{0} & \mathbf{G_{cd}}(s) & \mathbf{G_{c\omega}}(s)\\ \mathbf{G_{o\omega i,VI1}}(s) & \mathbf{0} & \mathbf{0}\end{bmatrix} \quad (22)$$

On the other hand, the modeling of the entire connection network is represented by (23). $\mathbf{G_{nwex}}(s)$ is the extended transfer function matrix from $\vec{Y}_{ex}(s)$ to $\vec{D}_{ex}(s)$, and is defined as the terminal-characteristics matrix model of the connection network. The expression of $\mathbf{G_{nwex}}(s)$ is shown in (24), where $\mathbf{G_{nw}}(s)$ is the traditional impedance matrix model of the connection network without considering the variation of the fundamental frequency ω^{s} [15], while $\mathbf{G_{nw\omega}}(s)$ is the fundamental-frequency-related terminal-characteristics matrix model of the connection network. $\mathbf{I}$ is the identity matrix. The proposed derivation of $\mathbf{G_{nw}}(s)$ and $\mathbf{G_{nw\omega}}(s)$ is presented in detail in Section IV-B.

$$\vec{D}_{ex}(s)=\mathbf{G_{nwex}}(s)\vec{Y}_{ex}(s) \quad (23)$$

$$\mathbf{G_{nwex}}(s)=\begin{bmatrix}\mathbf{G_{nw}}(s) & \mathbf{G_{nw\omega}}(s)\\ \mathbf{0} & \mathbf{I}\end{bmatrix} \quad (24)$$

By combining the composite model of all inverters and the model of the connection network, the overall system model based on the CCM can be established as (25). Fig. 9 illustrates the small-signal block diagram of the overall system, which resembles a multiple-input-multiple-output (MIMO) negative feedback system. Each inverter should be designed to be stable individually before system integration, so $\mathbf{G_{clex}}(s)$ is stable and the closed-loop transfer function matrix $[\mathbf{I}+\mathbf{G_{cdex}}(s)\mathbf{G_{nwex}}(s)]^{-1}$ determines the system stability. The return-ratio transfer function matrix $\mathbf{L_{ex}}(s)$ and the return-difference transfer function matrix $\mathbf{F_{ex}}(s)$ of the MIMO closed loop can be expressed in (26). The system model is established in the common system *d-q* frame, and there are totally seven inverters. Moreover, the common system fundamental frequency vector $\vec{\tilde{\omega}}^{s}$ is also considered. Therefore, the sizes of both $\mathbf{L_{ex}}(s)$ and $\mathbf{F_{ex}}(s)$ are 16-by-16.

$$\vec{Y}_{ex}(s)=\left[\mathbf{I}+\mathbf{G_{cdex}}(s)\mathbf{G_{nwex}}(s)\right]^{-1}\mathbf{G_{clex}}(s)\vec{U}_{ex}(s) \quad (25)$$

$$\mathbf{L_{ex}}(s)=\mathbf{G_{cdex}}(s)\mathbf{G_{nwex}}(s),\quad \mathbf{F_{ex}}(s)=\mathbf{I}+\mathbf{L_{ex}}(s) \quad (26)$$

B. Derivation of the Terminal-Characteristics Matrix of the Connection Network

To model the terminal-characteristics matrix of the connection network considering the variation of the

fundamental frequency, the terminal characteristics of passive components, such as the branches, *RL* loads and shunt capacitors in the ac microgrids, should also be derived.

For system planning, the internal control information of procured inverters is normally unavailable, so the terminal characteristics of inverters are obtained by measurement instead of analytical derivation. However, the parameters of passive components are available for system designers and the steady-state operating point, including current, voltage and power, of the system can be obtained by power flow analysis. Therefore, analytical modeling is a feasible way to acquire the terminal characteristics of passive components.

The complete small-signal block diagrams of passive components in the common system *d-q* frame are illustrated in Fig. 10. $\mathbf{Y_b}(s)$, $\mathbf{Y_{ld}}(s)$ and $\mathbf{Y_{Cp}}(s)$ are the *d-q* admittance matrices of a branch, a *RL* load and a shunt capacitor, respectively. $\mathbf{G_{i\omega b}}(s)$, $\mathbf{G_{i\omega ld}}(s)$ and $\mathbf{G_{i\omega Cp}}(s)$ are the fundamental-frequency-related terminal-characteristics matrices of a branch, a *RL* load and a shunt capacitor, as expressed in (27), (28) and (29), respectively. L_b, R_b, L_{ld} and R_{ld} are the inductances and resistances of the branch and the *RL* load, C_p is the shunt capacitance, and I_{bd}^s, I_{bq}^s, I_{ldd}^s, I_{ldq}^s, V_{Cpd}^s and V_{Cpq}^s are the steady-state values of the branch current, load current and shunt capacitor voltage in the common system *d-q* frame, respectively.

$$\mathbf{Y_b}(s)=\begin{bmatrix} L_b s+R_b & -\omega^s L_b \\ \omega^s L_b & L_b s+R_b \end{bmatrix}^{-1},\ \mathbf{G_{i\omega b}}(s)=\mathbf{Y_b}(s)\begin{bmatrix} L_b I_{bq}^s & 0 \\ -L_b I_{bd}^s & 0 \end{bmatrix} \tag{27}$$

$$\mathbf{Y_{ld}}(s)=\begin{bmatrix} L_{ld} s+R_{ld} & -\omega^s L_{ld} \\ \omega^s L_{ld} & L_{ld} s+R_{ld} \end{bmatrix}^{-1},\ \mathbf{G_{i\omega ld}}(s)=\mathbf{Y_{ld}}(s)\begin{bmatrix} L_{ld} I_{ldq}^s & 0 \\ -L_{ld} I_{ldd}^s & 0 \end{bmatrix} \tag{28}$$

$$\mathbf{Y_{Cp}}(s)=\begin{bmatrix} C_p s & -\omega^s C_p \\ \omega^s C_p & C_p s \end{bmatrix},\ \mathbf{G_{i\omega Cp}}(s)=\begin{bmatrix} -C_p V_{Cpq}^s & 0 \\ C_p V_{Cpd}^s & 0 \end{bmatrix} \tag{29}$$

The extended nodal admittance equation of the connection network is defined in (30), where $\mathbf{I_{sys}}$ is the current vector flowing into all nodes, $\mathbf{V_{sys}}$ is the voltage vector of all nodes, $\mathbf{Y_{sys}}$ is the nodal admittance matrix of the connection work and $\mathbf{G_{i\omega sys}}$ is the fundamental-frequency-related nodal terminal-characteristics matrix of the connection work. $\mathbf{Y_{sys}}$ can be easily derived as in the normal nodal admittance equation, while $\mathbf{G_{i\omega sys}}$ can be derived in (31). Assume the numbers of the nodes, the branches, the *RL* loads and the shunt capacitors are *M*, *N*, *L* and *K*, respectively. The mapping matrix $\mathbf{M_{net}}$ is of size $2M\times 2N$, and it maps the branches onto the nodes of the connection network. The elements of $\mathbf{M_{net}}$ are 2×2 identity matrix $\mathbf{I}$ for the branch current leaving the node or $-\mathbf{I}$ for the branch current entering the node or 2×2 zero matrix $\mathbf{0}$ if the specific branch is not connected to the node. The mapping matrix $\mathbf{M_{load}}$ of size $2M\times 2L$ maps the loads onto the nodes, and its elements are $\mathbf{I}$ if the specific load is connected to the node or $\mathbf{0}$ if the specific load is not connected to the node. The mapping matrix $\mathbf{M_{cap}}$ of size $2M\times 2K$ maps the shunt capacitors onto the nodes, which is similar to $\mathbf{M_{load}}$.

$$\mathbf{I_{sys}}=\mathbf{Y_{sys}}(s)\mathbf{V_{sys}}+\mathbf{G_{i\omega sys}}(s)\tilde{\omega}^s \tag{30}$$

$$\begin{cases} \mathbf{G_{i\omega sys}}=\mathbf{M_{net}}\mathbf{G_{i\omega bN}}+\mathbf{M_{load}}\mathbf{G_{i\omega ldL}}+\mathbf{M_{cap}}\mathbf{G_{i\omega CpK}} \\ \mathbf{G_{i\omega bN}}=\begin{bmatrix} \mathbf{G_{i\omega b1}} \\ \mathbf{G_{i\omega b2}} \\ \vdots \\ \mathbf{G_{i\omega bN}} \end{bmatrix},\ \mathbf{G_{i\omega ldL}}=\begin{bmatrix} \mathbf{G_{i\omega ld1}} \\ \mathbf{G_{i\omega ld2}} \\ \vdots \\ \mathbf{G_{i\omega ldL}} \end{bmatrix},\ \mathbf{G_{i\omega CpK}}=\begin{bmatrix} \mathbf{G_{i\omega Cp1}} \\ \mathbf{G_{i\omega Cp2}} \\ \vdots \\ \mathbf{G_{i\omega CpK}} \end{bmatrix} \end{cases} \tag{31}$$

Similar to the derivation method of the impedance matrix of the connection network presented in [15], the proposed method for the derivation of the terminal-characteristics matrix of the connection network also contains two steps.

Step 1: reserve only buses with inverter connections.

The current vector $\mathbf{I_{sys}}$ / voltage vector $\mathbf{V_{sys}}$ of all buses are decomposed into the current vector $\mathbf{I_m}$ / voltage vector $\mathbf{V_m}$ of buses with inverter connections and the current vector $\mathbf{I_n}$ / voltage vector $\mathbf{V_n}$ of buses without inverter connection. Then, (30) can be reformatted as a partitioned matrix equation in (32). $\mathbf{I_n}$ is a zero vector, so (32) can be simplified as (33), where $\mathbf{Y_{bus}}$ is the admittance matrix and $\mathbf{G_{i\omega bus}}$ is the fundamental-frequency-related terminal-characteristics matrix of the simplified connection network.

$$\begin{bmatrix} \mathbf{I_m} \\ \mathbf{I_n} \end{bmatrix}=\begin{bmatrix} \mathbf{Y_{mm}} & \mathbf{Y_{mn}} \\ \mathbf{Y_{nm}} & \mathbf{Y_{nn}} \end{bmatrix}\begin{bmatrix} \mathbf{V_m} \\ \mathbf{V_n} \end{bmatrix}+\begin{bmatrix} \mathbf{G_{i\omega m}} \\ \mathbf{G_{i\omega n}} \end{bmatrix}\tilde{\omega}^s \tag{32}$$

$$\begin{aligned} \mathbf{I_m}&=\left(\mathbf{Y_{mm}}-\mathbf{Y_{mn}}\mathbf{Y_{nn}}^{-1}\mathbf{Y_{nm}}\right)\mathbf{V_m}+\left(\mathbf{G_{i\omega m}}-\mathbf{Y_{mn}}\mathbf{Y_{nn}}^{-1}\mathbf{G_{i\omega n}}\right)\tilde{\omega}^s \\ &=\mathbf{Y_{bus}}\mathbf{V_m}+\mathbf{G_{i\omega bus}}\tilde{\omega}^s \end{aligned} \tag{33}$$

Step 2: separate buses connected with voltage-controlled inverters from buses with current-controlled inverters.

$\mathbf{I_m}$ and $\mathbf{V_m}$ are further partitioned into vectors $\mathbf{I_v}$ / $\mathbf{V_v}$ of buses connected with voltage-controlled inverters and vectors $\mathbf{I_c}$ / $\mathbf{V_c}$ of buses connected with current-controlled inverters, as expressed in (34) and (35), respectively. By rewriting (33) as (36), $\mathbf{I_v}$ and $\mathbf{V_c}$ can be solved as expressed in (37), where impedance matrix $\mathbf{G_{nw}}$ and the fundamental-frequency-related terminal-characteristics matrix $\mathbf{G_{nw\omega}}$ of the connection network are derived consequently.

$$\mathbf{I_m}^{\mathrm{T}}=\left[\mathbf{I_v}\ \vdots\ \mathbf{I_c}\right]^{\mathrm{T}}=\left[\tilde{i}_{t,\mathrm{VI1}}^s\ \ \tilde{i}_{t,\mathrm{VI2}}^s\ \ \tilde{i}_{t,\mathrm{VI3}}^s\ \ \tilde{i}_{t,\mathrm{VI4}}^s\ \vdots\ \tilde{i}_{t,\mathrm{CI1}}^s\ \ \tilde{i}_{t,\mathrm{CI2}}^s\ \ \tilde{i}_{t,\mathrm{CI3}}^s\right]^{\mathrm{T}} \tag{34}$$

$$\mathbf{V_m}^{\mathrm{T}}=\left[\mathbf{V_v}\ \vdots\ \mathbf{V_c}\right]^{\mathrm{T}}=\left[\tilde{v}_{t,\mathrm{VI1}}^s\ \ \tilde{v}_{t,\mathrm{VI2}}^s\ \ \tilde{v}_{t,\mathrm{VI3}}^s\ \ \tilde{v}_{t,\mathrm{VI4}}^s\ \vdots\ \tilde{v}_{t,\mathrm{CI1}}^s\ \ \tilde{v}_{t,\mathrm{CI2}}^s\ \ \tilde{v}_{t,\mathrm{CI3}}^s\right]^{\mathrm{T}} \tag{35}$$

$$\begin{bmatrix} \mathbf{I_v} \\ \mathbf{I_c} \end{bmatrix}=\begin{bmatrix} \mathbf{Y_{vv}} & \mathbf{Y_{vc}} \\ \mathbf{Y_{cv}} & \mathbf{Y_{cc}} \end{bmatrix}\begin{bmatrix} \mathbf{V_v} \\ \mathbf{V_c} \end{bmatrix}+\begin{bmatrix} \mathbf{G_{i\omega v}} \\ \mathbf{G_{i\omega c}} \end{bmatrix}\tilde{\omega}^s \tag{36}$$

$$\begin{aligned} \begin{bmatrix} \mathbf{I_v} \\ \mathbf{V_c} \end{bmatrix}&=\begin{bmatrix} \mathbf{Y_{vv}}-\mathbf{Y_{vc}}\mathbf{Y_{cc}}^{-1}\mathbf{Y_{cv}} & \mathbf{Y_{vc}}\mathbf{Y_{cc}}^{-1} \\ -\mathbf{Y_{cc}}^{-1}\mathbf{Y_{cv}} & \mathbf{Y_{cc}}^{-1} \end{bmatrix}\begin{bmatrix} \mathbf{V_v} \\ \mathbf{I_c} \end{bmatrix} \\ &+\begin{bmatrix} \mathbf{G_{i\omega v}}-\mathbf{Y_{vc}}\mathbf{Y_{cc}}^{-1}\mathbf{G_{i\omega c}} \\ -\mathbf{Y_{cc}}^{-1}\mathbf{G_{i\omega c}} \end{bmatrix}\tilde{\omega}^s=\mathbf{G_{nw}}\begin{bmatrix} \mathbf{V_v} \\ \mathbf{I_c} \end{bmatrix}+\mathbf{G_{nw\omega}}\tilde{\omega}^s \end{aligned} \tag{37}$$

C. Stability Analysis Based on the CCM and the GNC

Because the proposed system model based on the CCM and the terminal characteristics of inverters and the connection work in the common system *d-q* frame is a MIMO negative feedback system, the GNC [24] can be applied to it for low-frequency stability analysis related to the droop control and the dynamics of the fundamental frequency. Two stability

analysis methods are thus proposed here, and the low-frequency stability of Case 1 and Case 2 mentioned in Section III-B is analyzed as an example.

The first proposed stability analysis method is expressed in (38), by applying the eigenvalue-based GNC to the return-ratio matrix $\mathbf{L_{ex}}(s)$. $P(\ )$ means the number of right-half-plane (RHP) poles, $Z(\ )$ represents the number of RHP zeros, and $N_{(-1,\,j0)}(\ )$ is the net sum of anticlockwise encirclements of the critical point $(-1,\,j0)$ by the set of *characteristic loci* of the return-ratio matrix [15], [23].

$$Z\left(\mathbf{F_{ex}}\right)=P\left(\mathbf{L_{ex}}\right)-N_{(-1,j0)}\left(\mathbf{L_{ex}}\right)=-N_{(-1,j0)}\left(\mathbf{L_{ex}}\right)=0 \quad (38)$$

There are no RHP poles in $\mathbf{G_{nwex}}(s)$ thanks to the passive connection network. $\mathbf{G_{cdex}}(s)$ does not have RHP poles either, because each inverter should be designed to be stable under ideal external conditions. Therefore, $P(\mathbf{L_{ex}}) = 0$, and the system is stable if and only if $N_{(-1,\,j0)}(\mathbf{L_{ex}}) = 0$.

Because only $N_{(-1,\,j0)}(\mathbf{L_{ex}})$ is required for stability analysis, the detailed transfer function matrix of $\mathbf{L_{ex}}(s)$ is not needed, and the stability can be readily assessed by the frequency-dependent characteristics $\mathbf{L_{ex}}(j\omega)$. Moreover, $\mathbf{L_{ex}}(j\omega)$ can be obtained by the aforementioned measured terminal characteristics of inverters and the frequency response data $\mathbf{G_{nwex}}(j\omega)$ generated by the terminal characteristics transfer function matrix $\mathbf{G_{nwex}}(s)$ of the connection network, assuming the parameters of the connection network are known. $\mathbf{L_{ex}}(j\omega)$ has 16 frequency-dependent characteristic loci (λ_1 to λ_{16}).

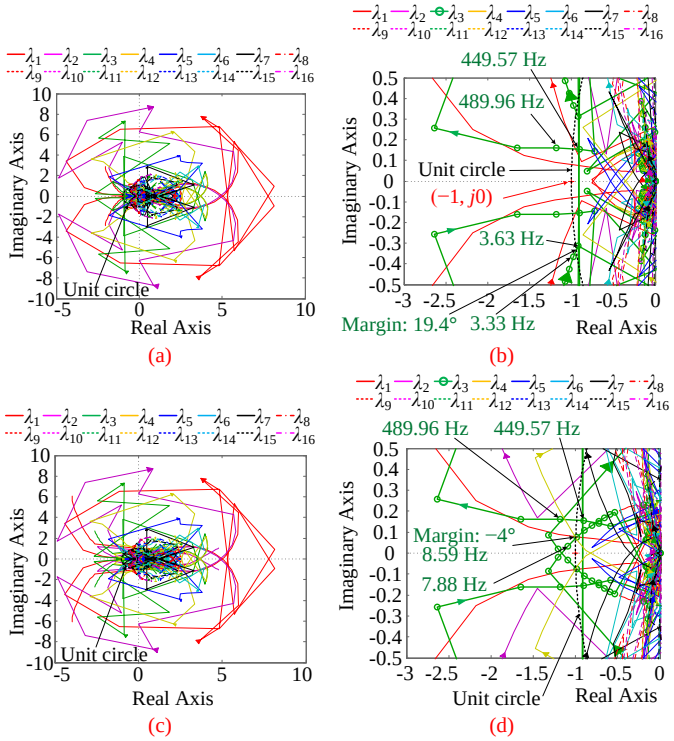

Fig. 11. (a) Full view and (b) zoomed-in view of characteristic loci of $\mathbf{L_{ex}}(j\omega)$ in Case 1. (c) Full view and (d) zoomed-in view in Case 2.

The characteristic loci of $\mathbf{L_{ex}}(j\omega)$ in both Case 1 and Case 2 are shown in Fig. 11. The characteristic loci do not encircle the critical point $(-1,\,j0)$ in Case 1, so $N_{(-1,\,j0)}(\mathbf{L_{ex}}) = 0$ and $Z(\mathbf{F_{ex}}) = 0$. In contrast, there are two clockwise encirclements of $(-1,\,j0)$ by the characteristic locus λ_3 in Case 2, and thus $N_{(-1,\,j0)}(\mathbf{L_{ex}}) = -2$ and $Z(\mathbf{F_{ex}}) = 2$. Therefore, according to the first proposed stability analysis method in (38), the microgrid is stable in Case 1 but unstable in Case 2 with two RHP poles. In Case 1, λ_3 intersects the unit circle at about 3.63 Hz and the phase margin is 19.4°, which implies damped oscillation. In Case 2, the frequency of the intersection point of λ_3 is about 8.59 Hz and the phase margin is −4°, which reveals unstable resonance.

The second proposed stability analysis method is expressed in (39), by applying the determinant-based GNC to the return-difference matrix $\mathbf{F_{ex}}(j\omega)$. det( ) denotes the *determinant*, and $N_{(0,\,j0)}(\ )$ means the number of anticlockwise encirclements of the origin point $(0,\,j0)$ by the Nyquist plot [15], [24]. The system is stable if and only if $N_{(0,\,j0)}(\det(\mathbf{F_{ex}}))$ is 0.

$$Z\left(\mathbf{F_{ex}}\right)=P\left(\mathbf{L_{ex}}\right)-N_{(0,j0)}\left(\det\left(\mathbf{F_{ex}}\right)\right)=-N_{(0,j0)}\left(\det\left(\mathbf{F_{ex}}\right)\right)=0 \quad (39)$$

The Bode plots of $\det(\mathbf{F_{ex}})$ in both cases are shown in Fig. 12. The approximate magnitude slope of −60dB/dec at 1 Hz implies that there are three integral elements in the system, so when drawing the Nyquist plot, the Nyquist trajectory segment corresponding to the infinitesimal semi-circle around the origin point in anti-clockwise direction of the Nyquist contour Γ_s in the s-plane ($[s]$) as depicted in Fig. 13(a) should be considered. Fig. 13(b) depicts the actual Nyquist plots of $\det(\mathbf{F_{ex}})$ in both cases, which is not convenient for counting the encirclements of $(0,\,j0)$, due to the large variations of magnitude and phase from 100 Hz to 1 kHz as evinced in Fig. 12. For the sake of checking the encirclements of $(0,\,j0)$ by the Nyquist plot, the angle difference between $\omega = 0^+$ and $\omega = +\infty$, in other words, net variation of angle in the full positive frequency range, is most important, and the large variation of phase between 100 Hz and 1 kHz can be neglected. Therefore, the simplified illustration of the Nyquist plots is presented in Fig. 13(c) to facilitate the explanation of encirclements of $(0,\,j0)$.

Alternatively, the Bode plots can also be used to determine the encirclements of $(0,\,j0)$. As shown in Fig. 12, the phase of $\det(\mathbf{F_{ex}})$ has 0° net variation in the full positive frequency range in Case 1 and thus $N_{(0,\,j0)}(\det(\mathbf{F_{ex}})) = 0$. But in Case 2, such net phase variation is $-180°\times2=-360°$ and hence $N_{(0,\,j0)}(\det(\mathbf{F_{ex}})) = -2$. Therefore, the proposed stability analysis method in (39) indicates that the microgrid is stable in Case 1 but unstable in Case 2 with two RHP poles. The proposed two stability analysis methods are consistent in the low-frequency stability analysis.

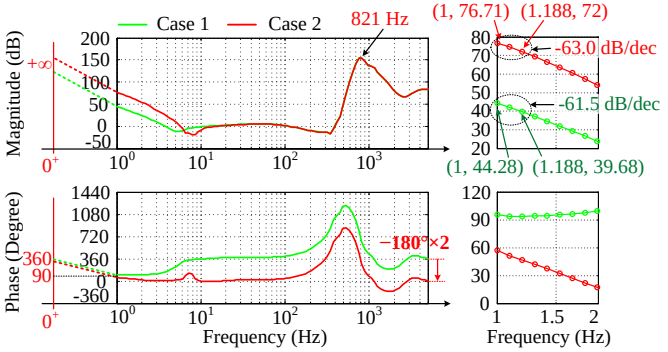

Fig. 12. Bode plots of $\det(\mathbf{F_{ex}}(j\omega))$ in both cases.

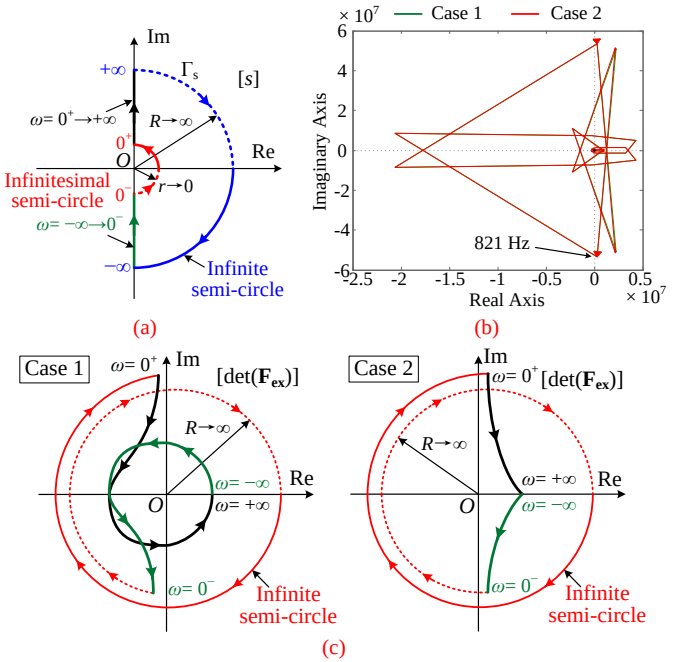

Fig. 13. (a) Nyquist contour Γ_s in the *s*-plane, (b) Nyquist plot of det($\mathbf{F}_{ex}$) and (c) simplified illustration of Nyquist plot of det($\mathbf{F}_{ex}$) when there are three integral elements in det($\mathbf{F}_{ex}$).

V. Simulation Verification

The inverter-based islanded multiple-bus ac microgrid described in Section II is simulated with MATLAB/Simulink. Both Case 1 and Case 2 are investigated by simulation.

A. Scenario 1: Change of the Operating Point

The initial values of droop controller parameters of inverters VI1−VI4 are m_P = 0.0025 and n_Q = 0.0067 as in Case 1. At first, the output active power and reactive power of each of inverters CI1−CI3 are 0, while inverters VI1−VI4 equally share the active power loads and each generates active power of 397 W. The grid fundamental frequency is 59.94 Hz.

At t_1=1 s, the output power of inverters CI1−CI3 is changed to follow the set point (P_0 =250 W and Q_0=150 Var) as listed in Table II. The output active power of each of inverters VI1−VI4 drops to 231 W, and the grid fundamental frequency shifts to 60.01 Hz. As shown in Fig. 14, the dynamic responses of the real power *P*, reactive power *Q*, fundamental frequency *f* and terminal voltage magnitude *V* of each inverter show quickly damped oscillations with a frequency of 3.7 Hz, which matches very well with the analysis result of 3.63 Hz in Section IV-C.

B. Scenario 2: Change of Droop Controller Parameters

As shown in Fig. 15, at t_2=2 s, the droop controller parameters are changed to m_P = 0.0050 and n_Q = 0.0133 as in Case 2, and the system exhibits unstable resonances. The major unstable resonance frequencies are 8 Hz and 8.5 Hz in the common system *d*-*q* frame, as revealed by the FFT analysis of *P*, *Q*, *f* and *V* of Inverter VI1. Fig. 16 further depicts the simulation waveforms of three-phase voltage v_{VI1} and current i_{VI1} of Inverter VI1 (a) with droop parameters in Case 1 and (b) during the change of droop parameters from Case 1 to Case 2. An obvious 8.5 Hz diverging oscillation in the magnitude of phase voltages and currents can be observed in Case 2, which agrees with the analysis result of 8.59 Hz in Section IV-C. The simulation results verify that the proposed stability analysis methods are effective in the low-frequency stability analysis of inverter-based islanded multiple-bus microgrids based on measured terminal characteristics of inverters in the common system *d*-*q* frame.

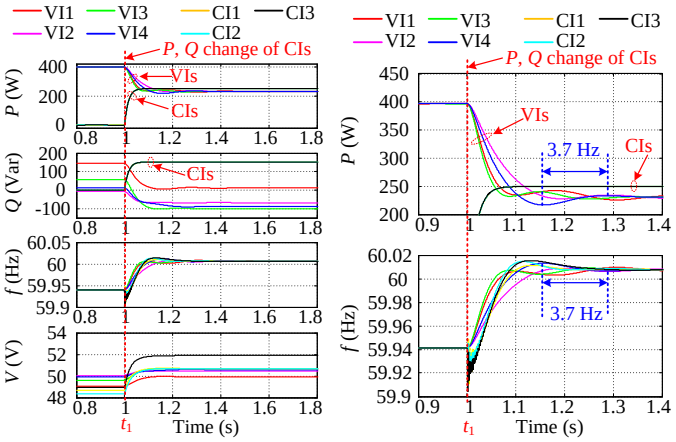

Fig. 14. Simulation results of the modified IEEE 37-bus system in the islanded mode in Case 1. (a) *P*, *Q*, *f* and *V* of seven inverters during the power change of CIs. (b) Zoomed-in waveforms of *P* and *f* during the power change.

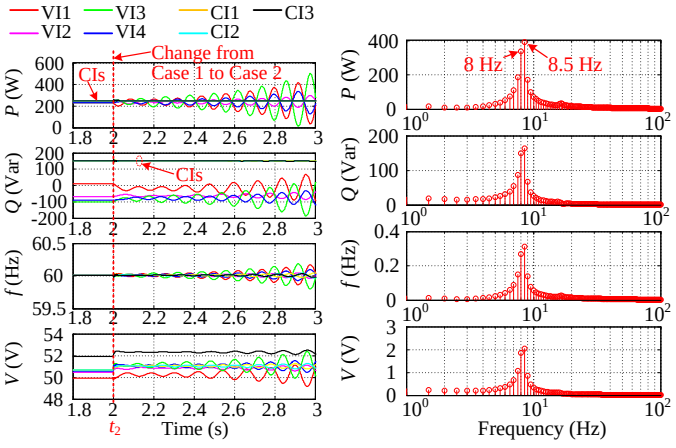

Fig. 15. Simulation results during the change from Case 1 to Case 2. (a) *P*, *Q*, *f* and *V* of seven inverters. (b) FFT analysis of *P*, *Q*, *f* and *V* of VI1 in Case 2.

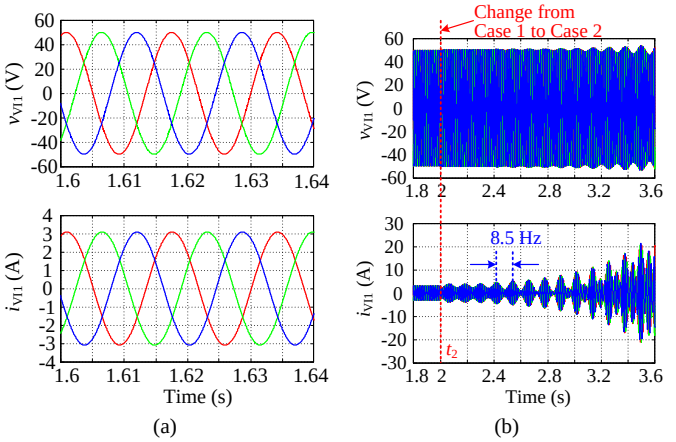

Fig. 16. Simulation waveforms of three-phase voltage v_{VI1} and current i_{VI1} of

Inverter VI1 (a) with droop parameters in Case 1 and (b) during the change of with droop parameters from Case 1 to Case 2.

VI. Discussion

A. Stability Analysis without Considering the Dynamics of Grid Fundamental Frequency

The stability analysis methods based on the CCM and the GNC presented in [15] for instability issues related to the medium and high frequency modes neglected the slow outer power sharing loops of inverters and assumed the grid fundamental frequency as constant. By applying this method in [15] to the studied IEEE 37-bus system in the islanded mode, the return-ratio matrix $\mathbf{L}_{no}(s)$ of the MIMO feedback loop of the CCM-based system model can be expressed as (40), where $\mathbf{G}_{cdno}(s)$ is the closed-loop transfer-function matrix from disturbance to output with the output impedances or admittances of all inverters as the diagonal elements, and $\mathbf{G}_{nwno}(s)$ is the MIMO impedance matrix of the connection network.

$$\mathbf{L}_{no}(s) = \mathbf{G}_{cdno}(s)\mathbf{G}_{nwno}(s) \tag{40}$$

Because $\mathbf{L}_{no}(j\omega)$ does not consider the dynamics of grid fundamental frequency, it only has 14 frequency-dependent characteristic loci (λ_1 to λ_{14}), as depicted by the Nyquist plots in Fig. 17 for Case 1. The intersection points of the characteristic loci of $\mathbf{L}_{no}(j\omega)$ and the unit circle only exhibit oscillatory modes in the medium-frequency range (that is, 409 Hz and 523 Hz) but cannot reveal the low-frequency oscillatory mode (3.7 Hz) observed in simulation Scenario 1.

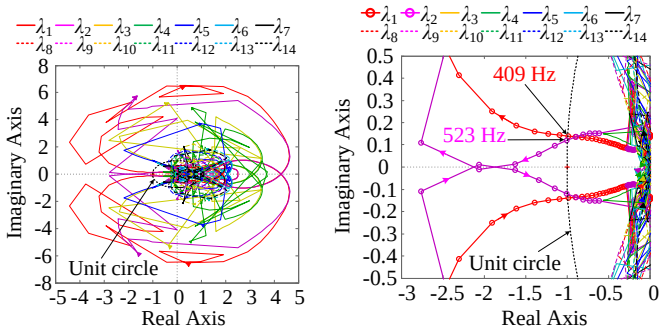

Fig. 17. (a) Full view and (b) zoomed-in view of characteristic loci of $\mathbf{L}_{no}(j\omega)$ in Case 1.

In contrast, the proposed stability analysis methods in this paper specifically consider the dynamics of the outer power sharing loops and include the grid fundamental frequency as an additional variable in the models of inverters and the system. The measurement of inverter terminal characteristics in this paper not only covers the traditional impedance and admittance in the low-frequency range, but also includes the fundamental-frequency-related terminal characteristics. The characteristic loci of $\mathbf{L}_{ex}(j\omega)$ explicitly discloses the low-frequency oscillatory mode (3.63 Hz), as shown in Fig. 11(b), which is consistent with the damped low-frequency oscillation Therefore, compared with the prior art [15] where the grid fundamental frequency is assumed as constant, the proposed methods have the benefit to the analysis of low-frequency oscillatory modes in droop-controlled ac microgrids.

B. Practical Implementation of the Proposed Methods

The procedure for practical implementation of the proposed stability analysis method for analysis of low-frequency stability in islanded multiple-bus ac microgrids during the installation stage can be described by the following steps.

Step 1: Gather the information of the planned ac microgrid, including:

1) the system topology,

2) the number, locations and operating modes (such as voltage-controlled mode, current-controlled mode, *P-Q* controlled mode, *P-V* controlled mode, etc.) of the inverters,

3) and the parameters (inductance, resistance and capacitance) of all passive components (such as branches, *RL* loads and shunt capacitors) inside the system.

Step 2: Arbitrarily choose the terminal *d-q* reference frame of one droop-controlled inverter as the common system *d-q* reference frame.

Step 3: Calculate the system steady-state operating point, including current, voltage and power of all inverters and passive components in the common system *d-q* reference frame, as well as the steady-state angle differences δ_0 between other inverter terminal *d-q* reference frames and the common system *d-q* reference frame, by using power flow analysis technique.

Step 4: Measure the terminal characteristics of all current-controlled inverters and droop-controlled inverters at their desired operating points in the common system *d-q* reference frame, by using the terminal-characteristics measurement technique presented in Section III-B. The recommended measurement frequency range starts from 1 Hz or even lower to cover the estimated droop control bandwidth and ends at half of the estimated switching frequency of procured inverters.

Step 5: Obtain the frequency response $\mathbf{G}_{cdex}(j\omega)$ of the extended closed-loop transfer function matrix from the disturbance to the output $\mathbf{G}_{cdex}(s)$, as expressed in (41) for the studied IEEE 37-bus system as an example, by combining the measured terminal characteristics of inverters.

$$\mathbf{G}_{cdex}(j\omega) = \begin{bmatrix} \mathbf{Z}_{ovp,VI1}(j\omega) & \mathbf{0} & \mathbf{0} \\ \mathbf{0} & \mathbf{G}_{cd}(j\omega) & \mathbf{G}_{c\omega}(j\omega) \\ \mathbf{G}_{o\omega i,VI1}(j\omega) & \mathbf{0} & \mathbf{0} \end{bmatrix} \tag{41}$$

Step 6: Derive the analytical terminal-characteristics transfer-function matrix $\mathbf{G}_{nwex}(s)$ of the connection network, by applying the method developed in Section IV-B, and get its frequency response $\mathbf{G}_{nwex}(j\omega)$ in the measured frequency range.

Step 7: Apply the proposed stability analysis methods described in Section IV-C to $\mathbf{G}_{cdex}(j\omega)$ and $\mathbf{G}_{nwex}(j\omega)$ to predict the stability of the planned ac microgrid at the desired system operating point.

For stability prediction at a different system operating point, the analysis process should restart at Step 3.

C. Benefits and Challenges of the Proposed Methods

The proposed stability analysis methods have the following benefits.

1) The dynamics of the grid fundamental frequency is included in the terminal characteristics of both inverters and passive components, so the proposed methods are of benefit to the analysis of low-frequency stability related with inverter droop control and fundamental frequency regulation, as compared with the prior art [15] assuming constant grid fundamental frequency.

2) The proposed methods only rely on the measured frequency responses of terminal characteristics of inverters, and thus they eliminate the need for the internal control information of procured commercial inverters, as compared with the state-space-based approach [2].

3) The proposed methods present a systematic approach to system modelling based on the CCM in the frequency domain with inverters clearly separated from the passive connection network. The terminal characteristics of inverters can be individually measured. The terminal-characteristics matrix of the passive connection network can be derived from the nodal admittance equation and simple matrix manipulation. The establishment of CCM-based system model and the application of the GNC stability criterion are only mathematical calculation of frequency response matrices. Such explicit system interpretation and basic mathematical calculation enable easy implementation in computer software, such as MATLAB and power system software to handle large system dimension. Therefore, the proposed methods are beneficial to stability analysis of complicated multiple-bus ac microgrids. In comparison, the stability analysis approaches presented in [18]–[20] are only applicable to single-bus microgrids.

The challenges in the practical application of the proposed methods are mainly with the hardware implementation of the inverter terminal characteristics measurement.

1) Traditional *d-q* impedance measurement still has some challenges, such as the measurement error introduced by the dynamics of the phase angle used for *d-q* reference frame transformation during perturbation injection and impedance calculation [26]. Measurement of fundamental-frequency-related terminal characteristics further requires the perturbation injection and response measurement of the common system fundamental frequency, so it is challenging how to improve the measurement accuracy.

2) The droop control determines that the terminal characteristics in the low-frequency range is closely related with the operating point, and thus terminal characteristics should be measured multiple times for all concerned operating points, which could involve large efforts.

VII. Conclusion

This paper proposes two stability analysis methods to analyze the low-frequency oscillation of the fundamental frequency in three-phase inverter-based islanded multiple-bus ac microgrids, based on the measured terminal characteristics of system components. The system modeling approach based on the CCM and the derivation method of the terminal-characteristics matrix of the connection network are proposed by including the fundamental frequency as an additional variable. The proposed stability analysis methods apply the GNC to the return-ratio and return-difference matrices of CCM-based system models. Simulation results verify that the proposed stability analysis methods can effectively assist microgrid planning in predicting the low-frequency stability related to the droop controllers and the system fundamental frequency, by using only the measured terminal characteristics of inverters without the need for their internal information.

References

[1] T. Morstyn, B. Hredzak, and V. G. Agelidis, "Control strategies for microgrids with distributed energy storage systems: an overview," *IEEE Trans. Smart Grid*, vol. 9, no. 4, pp. 3652–3666, Jul. 2018.

[2] N. Pogaku, M. Prodanovic, and T. C. Green, "Modeling, analysis and testing of an inverter-based microgrid," *IEEE Trans. Power Electron.*, vol. 22, no. 2, pp. 613–625, Mar. 2007.

[3] K. Yu, Q. Ai, S. Wang, J. Ni, and T. Lv, "Analysis and optimization of droop controller for microgrid system based on small-signal dynamic model," *IEEE Trans. Smart Grid*, vol. 7, no. 2, pp. 695–705, Mar. 2016.

[4] X. Wang, F. Blaabjerg, and W. Wu, "Modeling and analysis of harmonic stability in an ac power-electronics-based power system," *IEEE Trans. Power Electron.*, vol. 29, no. 12, pp. 6421–6432, Dec. 2014.

[5] A. Kahrobaeian and Y. A.-R. I. Mohamed, "Analysis and mitigation of low-frequency instabilities in autonomous medium-voltage converter-based microgrids with dynamic loads," *IEEE Trans. Ind. Electron.*, vol. 61, no. 4, pp. 1643–1658, Apr. 2014.

[6] N. Rashidirad, M. Hamzeh, K. Sheshyekani, and E. Afjei, "A simplified equivalent model for the analysis of low-frequency stability of multi-bus dc microgrids," *IEEE Trans. Smart Grid*, vol. 9, no. 6, pp. 6170–6182, Jul. 2018.

[7] P. Vorobev, P. H. Huang, M. A. Hosani, J. L. Kirtley, and K. Turitsyn, "High-fidelity model order reduction for microgrids stability assessment," *IEEE Trans. on Power Syst.*, vol. 33, no. 1, pp. 874–887, Nov. 2018.

[8] I. P. Nikolakakos, H. H. Zeineldin, M. S. El-Moursi, and J. L. Kirtley, "Reduced-order model for inter-inverter oscillations in islanded droop-controlled microgrids," *IEEE Trans. Smart Grid*, vol. 9, no. 5, pp. 4953–4963, Sep. 2018.

[9] Y. Wang, X. Wang, F. Blaabjerg, and Z. Chen, "Small-signal stability analysis of inverter-fed power systems using component connection method," *IEEE Trans. Smart Grid*, vol. 9, no. 5, pp. 5301–5310, Sep. 2018.

[10] B. Wen, D. Boroyevich, R. Burgos, P. Mattavelli, and Z. Shen, "Small-signal stability analysis of three-phase ac systems in the presence of constant power loads based on measured d-q frame impedances," *IEEE Trans. Power Electron.*, vol. 30, no. 10, pp. 5952–5963, Oct. 2015.

[11] M. Amin and M. Molinas, "Small-signal stability assessment of power electronics based power systems: a discussion of impedance- and eigenvalue-based methods," *IEEE Trans. Ind. Appl.*, vol. 53, no. 5, pp. 5014–5030, Sep./Oct. 2017.

[12] B. Wen, D. Boroyevich, R. Burgos, P. Mattavelli, and Z. Shen, "Analysis of d-q small-signal impedance of grid-tied inverters," *IEEE Trans. Power Electron.*, vol. 31, no. 1, pp. 675–687, Jan. 2016.

[13] M. Cespedes and J. Sun, "Impedance modeling and analysis of grid-connected voltage-source converters," *IEEE Trans. Power Electron.*, vol. 29, no. 3, pp. 1254–1261, Mar. 2014.

[14] W. Cao, Y. Ma, and F. Wang, "Sequence-impedance-based harmonic stability analysis and controller parameter design of three-phase inverter-based multi-bus ac power systems," *IEEE Trans. Power Electron.*, vol. 32, no. 10, pp. 7674–7693, Oct. 2017.

[15] W. Cao, Y. Ma, L. Yang, F. Wang, and L. M. Tolbert, "D-q impedance based stability analysis and parameter design of three-phase inverter-based ac power systems," *IEEE Trans. Ind. Electron.*, vol. 64, no. 7, pp. 6017–6028, Jul. 2017.

[16] G. Francis, R. Burgos, D. Boroyevich, F. Wang, and K. Karimi, "An algorithm and implementation system for measuring impedance in the

D-Q domain," in *Proc. IEEE Energy Convers. Congr. and Expo.*, 2012, pp. 3221–3228.

[17] Z. Shen, M. Jaksic, P. Mattavelli, D. Boroyevich, J. Verhulst, and M. Belkhayat, "Design and implementation of three-phase ac impedance measurement unit (IMU) with series and shunt injection," *Proc. Annu. IEEE Appl. Power Electron. Conf. and Expo.*, 2013, pp. 2674–2681.

[18] Z. Liu, J. Liu, D. Boroyevich, R. Burgos, and T. Liu, "Small-signal terminal-characteristics modeling of three-phase droop-controlled inverters," in *Proc. IEEE Energy Convers. Congr. and Expo.*, 2016, pp. 1–7.

[19] Z. Liu, J. Liu, and D. Boroyevich, "Small-signal terminal characteristics modeling of three-phase boost rectifier with variable fundamental frequency," in *Proc. Annu. IEEE Appl. Power Electron. Conf. and Expo.*, 2016, pp. 739–745.

[20] Z. Liu, J. Liu, D. Boroyevich, and R. Burgos, "Stability criterion of droop-controlled parallel inverters based on terminal-characteristics of individual inverters," in *Proc. IPEMC-ECCE Asia* 2016, pp. 2958–2963.

[21] S. Wang, Z. Liu, J. Liu, D. Boroyevich, and R. Burgos, "Small-signal modeling and stability prediction of parallel droop-controlled inverters based on terminal characteristics of individual inverters," *IEEE Trans. Power Electron.*, Early Access, 2019.

[22] Z. Yao, P. G. Therond, and B. Davat, "Stability analysis of power systems by the generalized Nyquist criterion," in *Proc. Int. Conf. Control*, Mar. 1994, vol. 1, pp. 739–744.

[23] M. Belkhayat, "Stability criterion for ac power systems with regulated loads," Ph.D. dissertation, Dept. Elect. Comput. Eng., Purdue University, West Lafayette, IN, USA, 1997.

[24] S. Skogestad and I. Postlethwaite, *Multivariable feedback control: analysis and design*. Hoboken, NJ: John Wiley, 2nd edition, 2005.

[25] L. Luo, and S. V. Dhople, "Spatiotemporal model reduction of inverter-based islanded microgrids," *IEEE Trans. Energy Convers.*, vol. 29, no. 4, pp. 823–832, Dec. 2014.

[26] H. Gong, D. Yang, and X. Wang, "Impact analysis and mitigation of synchronization dynamics for dq impedance measurement," *IEEE Trans. Power Electron.*, Early Access, 2018.